

Alma Mater Studiorum Università di Bologna
Archivio istituzionale della ricerca

Learning Nonlinear Electrical Impedance Tomography

This is the final peer-reviewed author's accepted manuscript (postprint) of the following publication:

Published Version:

Colibazzi F., Lazzaro D., Morigi S., Samore A. (2022). Learning Nonlinear Electrical Impedance Tomography. JOURNAL OF SCIENTIFIC COMPUTING, 90(1), 1-23 [10.1007/s10915-021-01716-4].

Availability:

This version is available at: <https://hdl.handle.net/11585/846336> since: 2022-10-25

Published:

DOI: <http://doi.org/10.1007/s10915-021-01716-4>

Terms of use:

Some rights reserved. The terms and conditions for the reuse of this version of the manuscript are specified in the publishing policy. For all terms of use and more information see the publisher's website.

This item was downloaded from IRIS Università di Bologna (<https://cris.unibo.it/>).
When citing, please refer to the published version.

(Article begins on next page)

This is the final peer-reviewed accepted manuscript of:

Colibazzi, F., Lazzaro, D., Morigi, S. *et al.* Learning Nonlinear Electrical Impedance Tomography. *J Sci Comput* 90, 58 (2022)

The final published version is available online at <https://dx.doi.org/10.1007/s10915-021-01716-4>

Terms of use:

Some rights reserved. The terms and conditions for the reuse of this version of the manuscript are specified in the publishing policy. For all terms of use and more information see the publisher's website.

This item was downloaded from IRIS Università di Bologna (<https://cris.unibo.it/>)

When citing, please refer to the published version.

Learning Nonlinear Electrical Impedance Tomography

Francesco Colibazzi* Damiana Lazzaro† Serena Morigi‡ Andrea Samoré§

Abstract

Electrical impedance tomography (EIT) is the problem of determining the electrical conductivity distribution of an unknown medium by making voltage and current measurements at the boundary of the object. The image reconstruction inverse problem of EIT is a nonlinear and severely ill-posed problem. The non-linear approach to this challenging problem commonly relies on the iterative regularized Gauss-Newton method, which, however, has several drawbacks: the critical choice of the regularization matrix and parameter and the difficulty in reconstructing step changes, as smooth solutions are favored. We address these problems by learning a data-adaptive neural network as the regularization functional and integrating a local anisotropic total variation layer as an attention-like function into an unrolled Gauss-Newton network. We finally show that the proposed learned non-linear EIT approach strengthens the Gauss-Newton approach providing robust and qualitatively superior reconstructions.

Keywords: nonlinear inverse problems; Electrical Impedance Tomography; sparsity-inducing regularization; unrolled optimization; anisotropic total variation.

1 Introduction

Electrical Impedance Tomography (EIT) is a nondestructive imaging technique that aims at reconstructing the inner conductivity distribution of a medium from a set of voltages registered on the boundary of the domain by a series of electrodes. This technique was developed in the early 1900s, to determine the distribution of electrical potential within the ground [24], but since then it has been adopted in a variety of fields, from medical imaging [20] and industrial process monitoring [22], to structural health monitoring [25] and tissue engineering [8],[5]. An integral part of EIT is the reconstruction algorithm which retrieves the conductivity distribution from boundary voltages. This can be formulated as an inverse conductivity problem, where the forward problem corresponds to the prediction of the voltages at electrode's location when the conductivity distribution and the injected current are known [2]. The forward problem has the form of an elliptic partial differential equation with Neumann boundary conditions, and it is usually solved with a finite element method.

The solution to the inverse EIT problem can be obtained by inverting the forward operator, the nonlinear mapping that characterizes the forward problem. The backprojection method, derived from the Radon transform and once commonly used in Computed Tomography, has been among the earliest numerical approaches, [23]. This approach, however, was associated with strong artifacts that severely impacted the reconstruction. For this reason the Landweber method [27], a modification of the generalized inverse matrix method, largely supplanted it. Despite the improvements that have followed over the years, the ill-posed nature of the EIT inverse problem still posed many challenges,

*Department of Mathematics, University of Bologna, Bologna, Italy. Email: francesco.colibazzi2@unibo.it.

†Department of Mathematics, University of Bologna, Bologna, Italy. Email: damiana.lazzaro@unibo.it.

‡Corresponding author. ORCID ID 0000-0001-8334-8798. Department of Mathematics, University of Bologna, Bologna, Italy. Email: serena.morigi@unibo.it.

§Department of Mathematics, University of Bologna, Bologna, Italy. Email: andrea.samore@unibo.it.

and meaningful reconstructions could often not be obtained, especially in the most common case of limited and noisy data. Regularization strategies proved to be essential to address this issue. Regularization methods constrain the space of possible reconstructions by embedding prior information about the expected structure of the domain. Among them, Total Variation (TV) promotes sparsity in the reconstructed distribution, thus favor piecewise constant (step changes) conductivities, while, Tikhonov regularization favours smooth solutions. Generalized Tikhonov methods make use of a smoothing penalty term that can include approximations of differential operators [16] or structural priors [26] to further improve reconstruction quality.

In addition to these model-based approaches, deep learning has recently become a new frontier of EIT and in general of inverse problems in imaging. Recent works for solving EIT inverse problems with deep learning focused on fully learned (end-to-end) and post-processing learned approaches. The former utilizes conventional neural networks as ‘black-box’ by feeding sufficiently large amount of training samples to learn the linear/non-linear mapping from the measured data to the target image without explicitly modeling the domain knowledge, i.e. the forward operator [4]. In this approach, the deep learning model must learn the underlying physics of the problem, which is difficult when the forward operator is nonlinear and not trivial as for EIT problems. Additionally, the ‘black-box’ nature of this approach makes it more difficult to identify erroneous solutions when the ground truth is not available, as the neural network will tend to produce reasonable solutions. Post-processing methods, on the other hand, are used after the reconstruction to remove artifacts and improve the result. As an example, in [10, 12] a deep learning based image post-processing is applied to the EIT result generated by D-bar direct method on the inverse Fourier domain [11]. While in [29], a cascaded end-to-end CNN, based on induced-current learning method (ICLM), processes the result of an approximated reconstruction computed by truncated singular value decomposition method. The effectiveness of these methods is however strongly linked to the success of the first reconstruction phase, as the deep learning is not used to integrate data driven knowledge into the regularization process.

In this work we present a *model-based data-learning* approach which aims at combining the advantages of model-based and data-driven paradigms. It relies on a physical forward model to describe the data generation, and on a prior model learned by data, that better promotes the desired features, while preserving the well-conditioning of the numerical problem. The key idea of the model-based data-learning proposal, inspired by many works on inverse imaging, consists in embedding a variational model in an unrolled iterative optimization algorithm which learns all the parameters for the prior model during the training procedure.

Unrolled optimization techniques consist of unfolding the iterative loop of a classical iterative algorithm with a given number of iterations and representing each iteration of the linearized version of the algorithm as processing layer of a neural network. This network can then be trained and optimized as any other network, learning from data while keeping the knowledge of the inverse problem in its internal structure. Unrolled architectures based on the linearized version of the most popular optimization algorithms have been successful in various inverse problems. Among them, the unrolled Gauss-Newton [30], Proximal Forward Backward Splitting [9], and Alternating Directions Method of Multipliers [21].

Following this framework, we unroll the iterative Gauss-Newton method, well assessed for optimizing a general nonlinear smooth model, to solve the inverse EIT nonlinear problem. This allows us to incorporate knowledge on the forward model into the neural network as well as directly optimize conductivity reconstruction quality based on training examples.

In addition, we introduce an attention-like strategy that can both sparsify the output of each iteration, driven by the structural anisotropic properties of the input. This feature has been inspired by Total-Variation Sparse Attention (TVMAX), a recently introduced attention mechanism to select visual attention over features generated by a CNN which further encourages the joint selection of

adjacent spatial locations [18]. We named the proposed mechanism Anisotropic Total Variation (ATV). Unlike TVMAX, ATV does not map all the probability mass onto a probability simplex, and does not rely on iterative forward computations. Although non-linear, ATV can be solved with a non-iterative algorithm, and we provide a closed-form expression for its Jacobian. This leads to an efficient implementation of its forward and backward steps.

ATV is then incorporated in each block of our unrolled Gauss-Newton EIT network as to transform non-linearly the output of the block and encourage structured and sparse attention over contiguous regions.

The work contents will be organized as follows. We introduce the mathematical formulations of the forward and inverse EIT problem in Section 2, and the Regularized Gauss-Newton (RGN) method for solving nonlinear least squares problems in Section 3. We formulate the proposed unrolled RGN network in Section 4 which contains numerical implementations details on the newly introduced regularizer network in Section 4.2, and on the ATV mechanism in Section 4.3. Numerical results are reported in Section 5, and, in Section 6, concluding remarks are presented.

2 EIT forward and inverse problem

In inverse EIT, small alternating currents are applied to conducting surface electrodes attached at the boundary of the object Ω . The measured voltages V_m on the electrodes are used to reconstruct electrical conductivity distribution σ of the internal part of the object.

In the corresponding forward EIT problem one wants to find the electric potential u in the interior of the object Ω and at the electrodes, given some applied current and inner conductivity σ . Following the accurate Complete Electrode Model (CEM), introduced in [7], the forward EIT problem can be formulated as follows:

$$\begin{cases} \nabla \cdot (\sigma(x) \nabla u(x)) = 0 & \text{in } \Omega, \\ u + z_l \sigma \frac{\partial u}{\partial n} = V_l & \text{on } E_l, l = 1, \dots, L, \\ \int_{E_l} \sigma \frac{\partial u}{\partial n} ds = I_l & \text{on } \Gamma, \\ \sigma \frac{\partial u}{\partial n} = 0 & \text{on } \tilde{\Gamma}, \end{cases} \quad (1)$$

where Γ ($\tilde{\Gamma}$) is the boundary $\partial\Omega$ with (without) electrodes, V_l is the unknown voltage to be measured by l -th electrode E_l when the currents I_l are applied, z_l are the contact impedances. The solution of forward EIT problem amounts to solving the boundary value problem (1).

The *Forward Operator* \tilde{F} , which operates between the Hilbert spaces X and Y , maps the conductivity σ to the solution of the forward problem:

$$\begin{aligned} \tilde{F}: \mathfrak{S} \subset X &\rightarrow Y \\ \sigma &\mapsto (u, V) \end{aligned} \quad (2)$$

where $\mathfrak{S} = \{\sigma \in L^\infty(\Omega) \mid \sigma \nabla u = 0\}$, denotes the domain of definition of \tilde{F} .

From now on we restrict the conductivities σ to a finite dimensional space of piecewise polynomials. We consider the object domain Ω discretized into n_T subdomains $\{\tau_j\}_{j=1}^{n_T}$ and σ constant over each of them. In particular we discretize Ω with a triangular mesh. Given a Finite Elements Model (FEM) of an EIT medium, we calculate the vector of voltages, V_m , for each FEM degree of freedom. For a given stimulation pattern a vector of n_M measurements is acquired, obtained by injecting current through an electrodes pair and then measuring the corresponding voltage V_m induced on another pair of electrodes. Then $F: \mathbb{R}^{n_T} \rightarrow \mathbb{R}^{n_M}$ represents the discrete version of the Forward Operator (2) as a

nonlinear vector map. Since \tilde{F} is Fréchet differentiable, F' is a matrix, called the Jacobian of F and denoted by J ; each element of $J \in \mathbb{R}^{n_M \times n_T}$ is defined as

$$\{J(u_d, u_m)\}_{i,j} = \int_{\tau_j} \nabla u_d \cdot \nabla u_m d\Omega, \quad (3)$$

where the row index i corresponds to the i th measurement, associated with the d th driving potential u_d and m th measurement potential u_m , while the column index j corresponds to the subdomain τ_j .

Considering measured data corrupted by additive noise, we can assume the following noisy non-linear observation model

$$V_m = F(\sigma) + \eta, \quad (4)$$

where $V_m \in \mathbb{R}^{n_M}$ represents the vector of all the measured electrode potentials whose dimension n_M depends on the choice of a measurement protocol, and $\eta \in \mathbb{R}^{n_M}$ is a zero-mean Gaussian distributed measurement noise vector.

Assuming the non-linear degradation model (4) and the given measurements V_m , the so called absolute imaging problem aims to estimate the (static) conductivity σ by solving the following **non-linear** least squares problem

$$\sigma^* = \arg \min_{\sigma} f(\sigma), \quad f(\sigma) = \int_{\Omega} (F(\sigma) - V_m)^2 d\Omega. \quad (\text{EITNL})$$

The underlying optimization problem is hard to solve, as the boundary currents depend non-linearly on the conductivity. This means that the optimization problem is nonconvex.

For the reconstruction of small conductivity changes, conventional approaches rely on the simplest linearized model of the non-linear forward operator F ,

$$F(\sigma) \approx F(\sigma_0) + J\delta\sigma = F(\sigma_0) + J(\sigma - \sigma_0), \quad (5)$$

where J represents the Jacobian matrix defined in (3), and calculated at the initial conductivity estimate σ_0 . The reconstruction is thus obtained by solving the following **linear** least squares problem

$$\delta\sigma^* = \arg \min_{\delta\sigma} f(\delta\sigma), \quad f(\delta\sigma) = \int_{\Omega} (J\delta\sigma - \delta V_m)^2 d\Omega, \quad (\text{EITL})$$

where $\delta\sigma = \sigma - \sigma_0$ and $\delta V_m = V_m - F(\sigma_0)$.

A benefit of the linear approach is that it leads to computationally fast reconstruction, however, the linearization leads to a very ill-conditioned undetermined linear system to solve, and the solution is only valid for sufficiently small deviations from the conductivity σ_0 at which the Jacobian is initially calculated.

We consider a two-dimensional convex domain Ω , where some inclusions with conductivity σ are embedded in a background material with conductivity σ_0 . In difference imaging the unknown conductivity to be reconstructed in the inversion model is the contrast $\sigma - \sigma_0$, i.e., conductivity change when the measurement data before the change is available; here σ_0 is the background conductivity. The proposed approach allows to reconstruct the absolute conductivity distribution when only the data after the change is available (σ_0 is not known).

3 Regularized Gauss-Newton for EITNL

The Gauss-Newton method is the most commonly used one for minimizing nonlinear least squares (NLS) problems such as the EITNL and performs a line search strategy with a specific choice of a descent direction. It simplifies the Newton-Raphson (NR) method which relies on the second-order

Taylor's expansion approximation of the function $f(\sigma)$. Specifically, the Newton-Raphson method approximates

$$f(\sigma + p) \approx f(\sigma) + \nabla f(\sigma)^T p + \frac{1}{2} p^T \nabla^2 f(\sigma) p, \quad (6)$$

where the gradient and the Hessian of $f(\sigma)$ are given respectively by

$$\nabla f(\sigma) = J(\sigma)^T (F(\sigma) - V_m), \quad \nabla^2 f(\sigma) = J(\sigma)^T J(\sigma) + \sum_k r_k(\sigma) \nabla^2 r_k(\sigma), \quad (7)$$

with $J(\sigma)$ the Jacobian matrix of $r(\sigma) := F(\sigma) - V_m$. The search direction p is computed by imposing optimality conditions for p to EITNL with $f(\sigma)$ approximated as in (6):

$$\frac{\partial f(\sigma + p)}{\partial p} = \nabla f(\sigma)^T + \nabla^2 f(\sigma) p = 0, \quad (8)$$

which implies that

$$\nabla^2 f(\sigma) p^{NR} = -\nabla f(\sigma). \quad (NR)$$

The Gauss-Newton method essentially approximates the Hessian matrix in (7) by ignoring all the second order terms from $\nabla^2 f(\sigma)$, so that the search direction p is obtained by solving the following linear system

$$J^T(\sigma) J(\sigma) p^{GN} = -J^T(\sigma) (F(\sigma) - V_m). \quad (GN)$$

Gauss-Newton method starts from an initial guess σ_0 and performs a line search along the direction p_k^{GN} to obtain the new conductivity iterate σ_{k+1} as

$$\sigma_{k+1} = \sigma_k + p_k^{GN}. \quad (9)$$

In (GN), V_m is the measurement vector, and the coefficient matrix, which involves the Jacobian matrix, is a linear operator. However, due to its compact nature, the operator has an unbounded (discontinuous) inverse. This causes the solution to be unstable against variations in the data, hence violating Hadamard's third criterion for well posedness. Therefore, applying the Gauss-Newton method to problem (EITNL) yields inaccurate solutions; one could instead employ some form of regularization on the sought solution σ . The regularized Gauss-Newton method, using a generalized Tikhonov regularizer, consists in applying GN to the minimization problem:

$$\sigma^* = \arg \min_{\sigma} \{ \mathcal{J}(\sigma; \lambda) = f(\sigma) + \lambda g(\sigma) \}, \quad g(\sigma) = \|L\sigma\|_2^2, \quad (10)$$

where $\lambda > 0$ is the regularization parameter, and $L \in \mathbb{R}^{n_T \times n_T}$ is a matrix representing either a discrete first/second order differential operator, or a positive diagonal matrix, or simply the identity matrix.

The gradient and the approximated Hessian matrix of the objective function in (10) are respectively given as follows:

$$\begin{aligned} \nabla \mathcal{J}(\sigma; \lambda) &= J(\sigma)^T (F(\sigma) - V_m) + \lambda L^T L \sigma, \\ \nabla^2 \mathcal{J}(\sigma; \lambda) &= \nabla^2 F(\sigma) (F(\sigma) - V_m) + J(\sigma)^T J(\sigma) + \lambda L^T L. \end{aligned} \quad (11)$$

The search direction p_k from the current iterate satisfies the linear system

$$(J(\sigma_k)^T J(\sigma_k) + \lambda L^T L) p_k^{\text{RGN-Tik}} = J(\sigma_k)^T (V_m - F(\sigma_k)) + \lambda L^T L \sigma_k. \quad (\text{RGN-Tik})$$

The Tikhonov-type regularization $g(\sigma)$ in (10), regardless of the choice of L , favors smooth solutions and fails in reconstructing step conductivity changes. A popular alternative to the Tikhonov regularizer, is the L_1 -norm Total Variation regularizer, defined as

$$g(\sigma) = \sum_i |(L\sigma)_i|, \quad (12)$$

with L in (12) the discrete gradient matrix. Replacing (12) in (10) enforces piecewise-constant conductivity reconstructions, and well preserves sharp conductivity changes, at the cost of a non-smooth optimization problem to solve. Recent TV regularized approaches to the EIT problem have provided efficient solutions to the non-differentiability: see [13] for nonlinear EIT problem solved via a forward-backward splitting strategy, [3] for a primal dual interior point method, [14] for an Alternating Direction Methods of Multipliers applied to linear EIT problems, and [1] for a simple lagged diffusivity method. Following [1], the approximate solution to the EIT problem (10) with a smoothed TV regularizer reads as

$$(J(\sigma_k)^T J(\sigma_k) + \lambda L^T E^{-1} L) p_k^{\text{RGN-TV}} = J(\sigma_k)^T (V_m - F(\sigma_k)) + \lambda L^T E^{-1} L \sigma_k, \quad (\text{RGN-TV})$$

where E is a diagonal matrix defined as $E := \text{diag}(\sqrt{(L\sigma)^2 + \gamma})$, and $\gamma > 0$ is the smoothing parameter.

Alternatively, the Levenberg-Marquardt algorithm directly regularizes the ill-conditioned linear system (GN) adding a scaled identity matrix λI , or even λL , to the coefficient matrix, thus improving its condition number. The approximate solution of the EIT non-linear problem is then given by

$$(J(\sigma_k)^T J(\sigma_k) + \lambda L^T L) p_k^{\text{LM}} = J(\sigma_k)^T (V_m - F(\sigma_k)). \quad (\text{LM})$$

The linear systems (RGN-Tik), (RGN-TV), and (LM) can be described by the following unified formulation

$$(J(\sigma_k)^T J(\sigma_k) + \lambda \mathcal{R}) p_k = b_k, \quad (\text{RGN})$$

where b_k is the associated right hand side and \mathcal{R} is a generic regularizer operator. Then the linear systems (RGN-Tik), (RGN-TV), and (LM) can be directly solved by

$$p_k = V_R \Sigma_R^{-1} U_R^T b_k, \quad (13)$$

where U_R , Σ_R , and V_R are given by the singular value decomposition (SVD) of the coefficient matrix in (RGN-Tik), (RGN-TV) or (LM).

Algorithm 1 RGN

Input: σ^0 , V_m , $\lambda > 0$,

Output: σ^* % conductivity distribution

For $k = 0, 1, \dots$, **do until convergence:**

 compute direction p_k by (13)

$\sigma_{k+1} = \sigma_k + p_k$

end

In Algorithm 1 we summarize the iterative steps of the regularized Gauss-Newton algorithm where the convergence is satisfied when two successive iterates differ for a given threshold.

The success of all these approaches is based on the critical choice of the λ regularization parameter, that is, on a long and painful exhaustive research that in practical applications is not in general sustainable.

3.1 Learning the regularization matrix

The a priori choice of the regularization operator $g(\sigma)$ in (RGN-Tik), (RGN-TV), and (LM), and the crucial selection of the regularization parameter λ can be avoided by learning automatically the regularizer from data, and simply setting $\lambda = 1$.

Let $J(\sigma_k) = U\Sigma V^T$ denote the SVD of $J(\sigma_k)$, where $U \in \mathbb{R}^{n_M \times n_M}$, and $V \in \mathbb{R}^{n_T \times n_M}$ are orthogonal matrices and $\Sigma \in \mathbb{R}^{n_M \times n_M}$ is the diagonal matrix which contains non-increasing singular values on the main diagonal. We construct the regularizer operator \mathcal{R}_θ as:

$$\mathcal{R}_\theta := V\Sigma_\theta V^T, \quad (14)$$

where Σ_θ , the diagonal matrix of singular values, will be learned by the network, as will be described in Section 4.2. Considering \mathcal{R}_θ in (14), and the decomposition $J^T J = V\Sigma^2 V^T$, then the linear system (RGN) can be rewritten as follows

$$(V\Sigma^2 V^T + V\Sigma_\theta V^T)p_k = J(\sigma_k)^T(V_m - F(\sigma_k)) + \mathcal{R}_\theta \sigma_k. \quad (15)$$

This choice for \mathcal{R}_θ allowed us to exploit the low-dimensional SVD for $J \in \mathbb{R}^{n_M \times n_T}$ instead of a more expensive SVD decomposition for the coefficient matrix in (RGN) of dimension $n_T \times n_T$ ($n_T \gg n_M$). Moreover, the solution p_k of the linear system reduces to the following matrix-vector product:

$$p_k = V(\Sigma^2 + \Sigma_\theta)^{-1}V^T(J(\sigma_k)^T(V_m - F(\sigma_k)) + \mathcal{R}_\theta \sigma_k). \quad (16)$$

4 Unrolled Iterative Regularized Gauss-Newton

Our goal is to iteratively solve (9)-(16) by executing a pre-determined number of iterations K of the regularized Gauss-Newton Algorithm 1, where the regularization operator $g(\sigma)$ is learned across a fully connected network. Moreover, the regularization parameter λ is avoided, so that to provide a parameter-free algorithmic approach to the nonlinear EIT problem. The resulting unrolled iterative architecture, named EITGN-NET, is depicted in Figure 1, and can be interpreted as a neural network which generates a sequence of approximated solutions σ_k , for $k = 1, \dots, K$, with $\sigma^* = \sigma_K$.

Starting with an initial guess σ_0 , the update mapping at a given iteration $k \in \{0, \dots, K-1\}$ reads as $\sigma_{k+1} \leftarrow \mathcal{G}(\sigma_k; J, V_m, \Sigma_\theta)$, where

$$\mathcal{G}(\sigma_k; J, V_m, \Sigma_\theta) := \sigma_k - (J(\sigma_k)^T J(\sigma_k) + \mathcal{R}_\theta)^{-1} r(\sigma_k) = \sigma_k - p_k \quad (17)$$

where $r(\sigma_k) = J(\sigma_k)^T(V_m - F(\sigma_k)) + \mathcal{R}_\theta \sigma_k$, and p_k is computed by solving (16).

The regularization operator \mathcal{R}_θ is a prior defined in (14) and computed by a Fully Connected Neural Network (FCNN). To encompass a large family of priors, we advocate a fully connected-based estimator \mathcal{R}_θ with weights θ , described in Section 4.2, that can be learned from historical (training) data.

The k -th iterative block \mathcal{L}_k corresponds to one iteration in algorithm RGN: first updates \mathcal{G} according to (17), and then combines the result with the ATV attention-like function to encourage piece-wise structures over contiguous regions on the intermediate reconstructions. In formulas, given an initial σ_0 , for $k = 1, \dots, K$ each block performs the following steps

$$\begin{cases} \bar{\sigma}_k = \mathcal{G}(\sigma_{k-1}; J, V_m, \Sigma_\theta) \\ \sigma_k = ATV(\bar{\sigma}_k). \end{cases} \quad (18)$$

The unrolled data flow is sketched in Algorithm 2. In the experiments reported in Section 5 we used $K = 10$, which provided a sufficiently good compromise between efficiency and accuracy in the reconstruction.

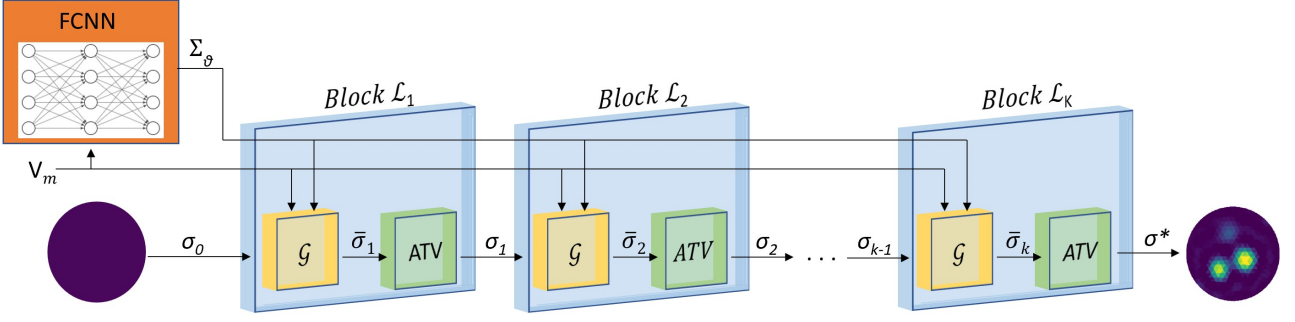


Figure 1: EITGN-NET architecture

Algorithm 2 EITGN-NET

Input: $\sigma^0, V_m,$

Output: σ^* % conductivity distribution

$\Sigma_\theta \leftarrow FCNN(V_m)$

For $k = 1, \dots, K$ **do:**

$\bar{\sigma}_k \leftarrow \mathcal{G}(\sigma_{k-1}; J, V_m, \Sigma_\theta)$

$\sigma_k \leftarrow ATV(\bar{\sigma}_k)$

end

$\sigma^* = \sigma_K$

end

The loss function used during the network training is defined in Section 4.1, while the regularization network to construct \mathcal{R}_θ , and the ATV layer will be described in Section 4.2 and Section 4.3, respectively.

4.1 Loss function design

In the network training process, EITGN-NET is applied on N_s training samples $\{V_m^{(i)}, \sigma_i^{GT}\}_{i=1}^{N_s}$ to obtain N_s reconstruction results σ_i^* . This allows for tuning the unknown parameters Θ of EITGN-NET defined in (25), by minimizing a loss function. Specifically, the loss function encodes both reconstruction and regularization costs and can be formulated as follows:

$$\begin{aligned} L_{tot}(\Theta) &= L_{rec} + L_{reg} \\ &= \frac{1}{N_s} \sum_{i=1}^{N_s} \|\sigma_i^* - \sigma_i^{GT}\|_2^2 + \frac{1}{N_s} \sum_{i=1}^{N_s} \|\mathcal{R}_\theta \sigma_i^*\|_2^2. \end{aligned} \quad (19)$$

The loss function L_{rec} measures how well the estimated conductivity distributions σ_i^* by the EITGN-NET matches the ground-truth ones σ_i^{GT} . The second term L_{reg} penalizes the network when the regularization contribution is too large, which could deviate from the original linear system to be solved.

Given the training samples and a loss function $L_{tot}(\Theta)$, the network EITGN-NET learns a parameter set Θ by iteratively training such that the loss functional (19) is minimized in Θ , by applying a gradient descent algorithm. Then the derivatives $\frac{\partial L_{tot}}{\partial \Theta^k}$ can be calculated by back-propagation technique using chain-rule

$$\frac{\partial L_{tot}}{\partial \Theta^k} = \frac{\partial L_{tot}}{\partial \bar{\sigma}_k} \cdot \frac{\partial \bar{\sigma}_k}{\partial \Theta^k} = \frac{\partial L_{tot}}{\partial \bar{\sigma}_k} \cdot \frac{\partial \bar{\sigma}_k}{\partial \Theta^k}. \quad (20)$$

Considering the functional operator on a generic block k given by (18), we have

$$\frac{\partial L_{tot}}{\partial \bar{\sigma}_k} = \sum_{k=1}^K \frac{\partial L_{tot}}{\partial ATV_k} \cdot \frac{\partial ATV_k}{\partial \bar{\sigma}_k}, \quad (21)$$

where $\frac{\partial L_{tot}}{\partial ATV_k}$ is in the backward propagation stage, and $\frac{\partial ATV_k}{\partial \bar{\sigma}_k}$ will be defined in (35).

4.2 Regularizer network

The regularization matrix \mathcal{R}_θ is constructed starting from its singular values Σ_θ following (14), by learning Σ_θ across a fully connected regression network $FCNN(V_m)$ consisting of four hidden layers each composed of n_M neurons. The input layer is initialized with the n_M measurement values V_m , and the output layer has n_M nodes that represent the sorted singular value vector Σ_θ .

In a fully connected network each neuron of a given layer has a connection (or synapse) towards each neuron of the next layer. For a given artificial neural node i , let there be m inputs, x_1 through x_m , and weights $\theta_{i,1}$ through $\theta_{i,m}$. The output of the i th neuron is:

$$y_i = \phi_1\left(\sum_{j=1}^m \theta_{i,j} x_j + b_i\right)$$

where ϕ_1 is the LeakyReLU activation function, defined as $LeakyReLU(z) = \max(\alpha_1 z, z)$, with a negative region slope of $\alpha_1 = 0.5$. For the output layer the function ϕ_1 is replaced by ϕ_2 which is the Rectified Linear Unit (ReLU) activation function

$$ReLU(z) = \max(\alpha_2, z + \alpha_2), \quad (22)$$

with translation factor $\alpha_2 = 1 \times 10^{-9}$. The output vector of each layer ℓ can be represented as

$$y^{[\ell]} = \phi_1(W^{[\ell]}x + b^{[\ell]}), \quad (23)$$

where the matrix $W^{[\ell]} \in \mathbb{R}^{n_M \times n_M}$ and the vector $b^{[\ell]} \in \mathbb{R}^{n_M}$, are the weights and the bias of the ℓ th layer. Hence the FCNN output is a vector

$$\Sigma_\theta(\theta; V_m) = \phi_2(\phi_1(W^{[5]}(\phi_1(W^{[4]}(\phi_1(W^{[3]}(\phi_1(W^{[2]}(\phi_1(W^{[1]}V_m + b^{[1]}) + b^{[2]}) + b^{[3]}) + b^{[4]}) + b^{[5]}), \quad (24)$$

where the set of weights and bias is denoted by

$$\Theta = \{W^{[1]}, W^{[2]}, W^{[3]}, W^{[4]}, W^{[5]}, b^{[1]}, b^{[2]}, b^{[3]}, b^{[4]}, b^{[5]}\}. \quad (25)$$

The choice of ϕ_2 as defined in (22) guarantees the non-singularity of Σ_θ and of the associated coefficient matrix in (15).

4.3 2D-Mesh anisotropic TV attention-like mechanism

The proposed attention-like mechanism, named ATV, acts inbetween the blocks of the EITGN-NET. It is derived by extending the total variation image denoising algorithm introduced in [15] to an arbitrary 2D triangular mesh domain.

The ATV mechanism operates on a 2D domain represented by a triangular mesh. Before discussing the proposed ATV operator, we introduce some notations and we formulate the total variation operator on a 2D mesh. Let us assume a planar domain $\Omega \subset \mathbb{R}^2$ which is approximated by a triangulated mesh (V, T, E) , where $V \in \mathbb{R}^{n_V \times 2}$, $V = \{v_i\}_{i=1}^{n_V}$ represents the set of vertices, $T \in \mathbb{R}^{n_T \times 3}$, $T = \{\tau_m\}_{m=1}^{n_T}$ is the set of triangles and $E \in \mathbb{R}^{n_E \times 2}$, $E = \{e_j\}_{j=1}^{n_E}$ is the set of edges.

We denote by $\mathcal{N}(\tau_i) = \{\tau_j \in T : \tau_j \cap \tau_i \in V\}$ the set of the triangles $\tau_j \in T$ which share one of their vertices or edges with the triangle τ_i . A basic $\mathcal{N}(\tau_i)$ could simply consider the edge intersection, thus reducing the cardinality of $\mathcal{N}(\tau_i)$ to 3 for inner triangles and 2 for boundary triangles.

We assume a piece-wise constant strictly bounded measurable function $\sigma : \Omega \rightarrow \mathbb{R}$ over the mesh triangles, thus the gradient operator vanishes to zero everywhere but the mesh edges along which it is constant. In particular, the discrete anisotropic gradient magnitude $\|(\nabla\sigma)_i\|_1$ on a triangle τ_i is defined as a weighted sum over the neighborhood triangles in $\mathcal{N}(\tau_i)$ as follows

$$\|(\nabla\sigma)_i\|_1 := \sum_{k \in \mathcal{N}(\tau_i)} w_k |\sigma_i - \sigma_k|, \quad i = 1, \dots, n_T, \quad (26)$$

where each weight w_k is associated to the triangle neighbor $\tau_k \in \mathcal{N}(\tau_i)$, and is defined as:

$$w_k = \frac{1}{\|barycentre(\tau_k) - barycentre(\tau_i)\|_2}. \quad (27)$$

We notice that (26) approximates the local variation of σ as sum of the weighted variations in each neighbors direction, thus discretizing an anisotropic total variation operator.

For a given triangle τ_i , we assume to know the values $\bar{\sigma}_k$ for all the neighbors in $\mathcal{N}(\tau_i)$, then the unknown value σ at τ_i is obtained as solution of the following local minimization problem:

$$\sigma^* = ATV(\sigma) := \arg \min_{\sigma \in \mathbb{R}} \mathcal{F}(\sigma), \quad \mathcal{F}(\sigma) := \sum_{k \in \mathcal{N}(\tau_i)} w_k |\sigma - \bar{\sigma}_k| + \mu |\sigma - \bar{\sigma}_i|^2, \quad i = 1, \dots, n_T. \quad (28)$$

The proposed ATV carries out the triangle-wise anisotropic TV, by solving the optimization problem (28) for any triangle τ_i . In Proposition 1, following [15], we report the explicit solution of the local optimization problem (28).

Proposition 1. *Let τ be a generic triangle with n the cardinality of $\mathcal{N}(\tau)$. Assuming $w_k > 0$ be the weight defined in (27) and associated to $\tau_k \in \mathcal{N}(\tau)$, the values $\bar{\sigma}_k$ on $\tau_k \in \mathcal{N}(\tau)$ be sorted as $\bar{\sigma}_1 \leq \bar{\sigma}_2 \leq \dots \leq \bar{\sigma}_n$. Then the minimizer of problem (28) is given by $\sigma^* \in \mathbb{R}$ which is the unique minimizer of the anisotropic total variation problem*

$$\sigma^* = \arg \min_{\sigma \in \mathbb{R}} \mathcal{F}(\sigma) = median\{\bar{\sigma}_1, \dots, \bar{\sigma}_n, \bar{\sigma}_i + \frac{1}{2\mu}W_0, \bar{\sigma}_i + \frac{1}{2\mu}W_1, \dots, \bar{\sigma}_i + \frac{1}{2\mu}W_n\}, \quad (29)$$

where

$$W_j = -\sum_{k=1}^j w_k + \sum_{k=j+1}^n w_k, \quad j = 0, \dots, n. \quad (30)$$

The ATV optimization problem (28) is solved by applying the closed formula (29) on the 2D-mesh, as outlined in Algorithm 3. The median value computation in the algorithm could represent a computational bottleneck. However, this computation becomes cheap by using the smart strategy proposed in [15].

Algorithm 3 ATV

Input: $\bar{\sigma} \in \mathbb{R}^{n_T}$, $\mu > 0$,**Output:** $\sigma^* \in \mathbb{R}^{n_T}$ Initialize $\sigma = \bar{\sigma}$ **For** each $\tau_i \in T$ **do**: compute $W \in \mathbb{R}^{n+1}$ as in (30) set $u = (\sigma_0, \dots, \sigma_{i-1}, \sigma_{i+1}, \dots, \sigma_n) \in \mathbb{R}^n$ $u \leftarrow \text{sort}(u)$ in ascending order compute $p \in \mathbb{R}^{n+1}$, with $p_k = \sigma_i + \frac{1}{\mu}W_k$, $k = 0, \dots, n$ $\sigma_i^* \leftarrow \text{median}(u_1, u_2, \dots, u_n, p_0, p_1, p_2, \dots, p_n)$ **end****end**

Note that Algorithm 3 realizes a local anisotropic total variation. The result in Proposition 2 guarantees instead that, by iterating Algorithm 3, the convergence to the global anisotropic total variation is guaranteed. The attention module here proposed applies local ATV using only Algorithm 3, and thus does not need any iterative procedure to converge.

Proposition 2. *The algorithm ATV repeated until convergence, defines the vector $\sigma^* = (\sigma_1^*, \dots, \sigma_{n_T}^*) \in \mathbb{R}^{n_T}$ which is the global minimizer of the anisotropic total variation problem*

$$\sigma^* = \arg \min_{\sigma \in \mathbb{R}^{n_T}} \|\nabla \sigma\|_1 + \mu \|\sigma - \bar{\sigma}\|_2^2. \quad (31)$$

Proof. By iterating (28) j times for the ℓ th component $\sigma_\ell^{(j)}$, we get $\sigma_\ell^{(j+1)} = \arg \min_{\sigma_\ell \in \mathbb{R}} \mathcal{F}^{(j)}(\sigma_\ell)$. Hence

$$\mathcal{F}^{(j)}(\sigma_\ell^{(j+1)}) \leq \mathcal{F}^{(j)}(\sigma_\ell^{(j)}). \quad (32)$$

This implies that the energy over all triangles decreases, that is

$$\mathcal{F}(\sigma^{(j+1)}) \leq \mathcal{F}(\sigma^{(j)}), \quad (33)$$

and since it is also bounded from below, the sequence $\mathcal{F}(\sigma^{(j)})$ converges.

From Lemma 3.1 in [15], we have

$$|\sigma^{(j)} - \sigma^{(j+1)}| \leq \sqrt{\frac{\mathcal{F}(\sigma^{(j)}) - \mathcal{F}(\sigma^{(j+1)})}{\mu}}. \quad (34)$$

Therefore $\sigma^{(j)}$ converges to the vector $\sigma^* \in \mathbb{R}^{n_T}$. \square

In order to apply the $ATV(\sigma)$ attention-like mechanism in a neural network trained by backpropagation, two problems must be addressed. The first is the forward computation: how to evaluate $ATV(\sigma)$, i.e., how to solve the optimization problem in (28). The second is the backward computation: how to evaluate the Jacobian of $ATV(\sigma)$. The forward computation is solved by the closed-form (29). For the backward computation the main challenge is how to compute the derivatives of $ATV(\sigma)$. Note that ATV is smooth everywhere except on the (zero-measure) set of non-differentiable points. In particular, on a triangle τ_i , the partial derivative of ATV are defined as

$$\frac{\partial ATV}{\partial \bar{\sigma}_i} = \sum_{k \in \mathcal{N}(\tau_i)} w_k \text{sign}(\sigma - \bar{\sigma}_k) + 2\mu(\sigma - \bar{\sigma}_i), \quad (35)$$

which simplifies as follows

$$\frac{\partial ATV}{\partial \bar{\sigma}_i} = \begin{cases} 2k - n + 2\mu(\sigma^* - \bar{\sigma}_k) & \text{if } \bar{\sigma}_k < \sigma^* < \bar{\sigma}_{k+1} \\ \ell + (m - \ell)\epsilon - (n - m) + 2\mu(\sigma^* - \bar{\sigma}_i) & \text{if } \bar{\sigma}_\ell < \bar{\sigma}_{\ell+1} = \dots = \bar{\sigma}_m = \sigma^* < \bar{\sigma}_{m+1} \end{cases} \quad (36)$$

The bottom condition in (36) corresponds to the case σ^* coincides with one of the $\bar{\sigma}_k$. In this case ϵ satisfies

$$\epsilon = \begin{cases} 1 & \text{if } i \leq \ell, \\ p \in [-1, 1] & \text{if } \ell + 1 \leq i \leq m, \\ -1 & \text{if } i > m. \end{cases} \quad (37)$$

The backpropagation task in (20) is then completed by using (36).

5 Simulations and Numerical Experiments

To evaluate the performance of the proposed network, a series of numerical and experimental tests was conducted on a set of synthetic 2D experiments. All examples simulate a circular tank slice of unitary radius represented by a mesh grid of 660 triangles. In the circular boundary ring 16 electrodes are equally spaced located. The conductivity of the background liquid is set to be $\sigma_0 = 1.0 \Omega m^{-1}$. Measurements are simulated through *opposite injection - adjacent measurement* protocol via pyEIT [17] a python based framework for Electrical Impedance Tomography. In all the examples the setup is considered blind, that is no a priori information about the sizes or locations of the inclusions is considered.

In the examples illustrated in Section 5.4-5.6 we compare the performance of the proposed EITGN-NET with the iterative Regularized Gauss Newton method (RGN), and the Levenberg Marquardt (LM) implemented using pyEIT library, and the D-bar method [19], with code kindly provided by the authors. The D-bar output is provided and visualized in image form, suitably handled for comparisons. The comparisons are conducted qualitatively by visually inspecting the artifacts and quantitatively by calculating the metrics described in Section 5.2 such as mean-square error (MSE), structural similarity (SSIM), dynamic range (DR), and the evaluation index for EIT images (EIEI). In all the experiments with RGN and LM algorithms, we hand-tuned the regularization parameter λ so as to fairly achieve the best performance in terms of MSE values.

The learning rate is set to 10^{-3} . The learning is performed for 20 epochs. The network is implemented on a PC with Intel i7 CPU and 32-GB RAM with Pytorch and AdamW has been used for optimization. The training process took nearly 30min each epoch of the training.

5.1 Training and Testing Data Sets

In the training process, we employed 250 randomly generated test cases, where 200 of them were used as training dataset and the other 50 test cases were used as testing dataset. Experimentally, we found that 20 epochs were enough to sufficiently decrease the total loss function. The collected weights Θ at epoch 20 have been used in EITGN-NET in the testing phase.

A training dataset contains a total number of 200 pairs of the ground-truth conductivity σ^{GT} and their corresponding collected voltages, V_m . Each test case consists of a random number from 1 to 4 of anomalies inside a circular tank, localized randomly and characterized by random radius in the range $[0.15 - 0.25]$ and magnitude in the range $[0.2, 2]$. Here it is assumed that each actual anomaly approximately consists of the same material, while the background consists of another homogeneous material. Consequently, a preferable EIT reconstruction meets the following conditions: C1) Anomalies of homogeneous material must have the same intensity. C2) Anomalies and backgrounds have higher and lower intensities than those of artifacts, respectively. C3) The number of triangles partitioned into the cluster of artifacts should be as small as possible.

5.2 Figures of merit

The performance is assessed both qualitatively and quantitatively. The quantitative analysis is performed on the mesh elements, via the Mean Squared Error (MSE) defined as

$$MSE_\sigma = \frac{\|\sigma^{GT} - \sigma^*\|_2^2}{n_T}, \quad (38)$$

which measures how well the original conductivity distribution is reconstructed in case a ground truth conductivity distribution σ^{GT} is known.

Another metric commonly used for measuring the similarity between two images is the Structural SIMilarity (SSIM) Index, which has been suitably modified to act directly on a mesh. In particular, local $SSIM_{\tau_i}$ measures are computed on local neighborhoods $\mathcal{N}(\tau_i)$, which move triangle by triangle on the entire mesh Ω . In other words, for each triangle τ_i , the $SSIM_{\tau_i}$ is calculated on its neighborhood. The global structural similarity measure SSIM between a reconstructed conductivity σ^* and the corresponding ground truth σ^{GT} is defined as follows

$$SSIM(\sigma^{GT}, \sigma^*) := \frac{1}{n_T} \sum_{i=1}^{n_T} SSIM_{\tau_i}(\sigma_i^{GT}, \sigma_i^*), \quad (39)$$

where for each triangle i th,

$$SSIM_{\tau_i}(\sigma_i^{GT}, \sigma_i^*) = \frac{(2\mu_i^{GT}\mu_i^* + c_1)(2s_i^{GT*} + c_2)}{((\mu_i^{GT})^2 + (\mu_i^*)^2 + c_1)((s_i^{GT})^2 + (s_i^*)^2)}, \quad (40)$$

with μ_i denotes the mean of the σ values in the neighbors $\mathcal{N}(\tau_i)$ of the triangle τ_i , s_i represents its associated standard deviation

$$s_i^{GT*} := \frac{1}{|\mathcal{N}(\tau_i)|} \sum_{k \in \mathcal{N}(\tau_i)} (\sigma_k^{GT} - \mu_k^{GT})(\sigma_k^* - \mu_k^*)$$

and finally $c_1 = \max(\sigma^{GT}) * 0.01^2$ and $c_2 = \max(\sigma^{GT}) * 0.03^2$.

Analogously to the use in image processing, $SSIM(X, Y)$ in (39) quantifies how much X and Y are different, with $SSIM = 1$ if X and Y are identical and $SSIM$ tends toward 0 when X and Y are very different.

According to conditions C1)-C2)-C3) the quality of any EIT reconstruction will increase as the number of artifact values decreases. In [28] an ad hoc evaluation index for EIT (Evaluation Index Electrical Impedance - EIEI-) has been introduced, which measures the homogeneity of the anomalies. Let n_1 be the number of triangles of backgrounds, with associated values denoted by $\sigma^{(1)}$, n_2 the number of triangles classified as artifacts, with associated values $\sigma^{(2)}$, and n_3 the number of triangles containing anomalies, with associated values $\sigma^{(3)}$. Unlike in [28], in our work the anomalies can have different values, thus we adapted the clusterization phase, accordingly. The variances of these clusters are given by

$$\delta_j = \sum_{i=1}^{n_j} |\sigma_i^{(j)} - \bar{\sigma}^{(j)}| / n_j, \quad j = 1, 2, 3. \quad (41)$$

The values of variances reflect the homogeneity of backgrounds, anomalies and artifacts. Then the EIEI measure is defined as follows

$$EIEI := w_1 T_1 + w_2 T_2 \quad (42)$$

with $T_1 := 1 - n_2/n_T$ the quantity of artifact triangles, $T_2 := 1 - (\delta_1 n_1/n_T + \delta_3 n_3/n_T)$, the quantity of background and anomalies, the weighting values w_1 and w_2 represent the certainty of T_1 and T_2 ,

Blocks (K)	8	10	12
MSE	0.0039	0.0037	0.0038
SSIM	0.87	0.89	0.89

Table 1: Effect of a different numbers of blocks K in the unrolled iterative EITGN-NET.

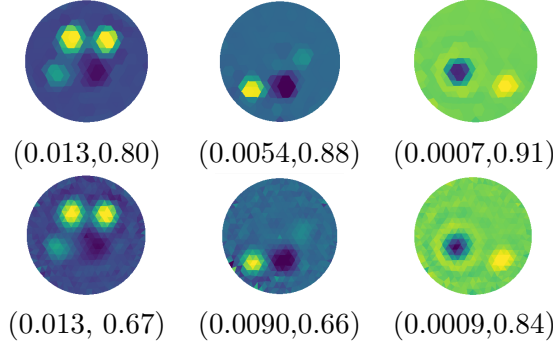


Figure 2: First row: EITGN-NET with ATV. Second row: EITGN-NET without ATV. (MSE, SSIM) values are reported for each test cases GT 225, GT 226, GT 232.

which is evaluated as

$$w_1 := \sum_{i=1}^{n_2} \sigma_i^{(2)} / n_2, \quad w_2 := \left(\sum_{i=1}^{n_1} \sigma_i^{(1)} + \sum_{i=1}^{n_3} \sigma_i^{(3)} \right) / (n_1 + n_3). \quad (43)$$

Together with the quantitative EIEI measure defined in (42), this figure of merit allows for a qualitative insight provided by a structure maps (EIEI map) where yellow color identifies the artefacts, red color the anomalies and blue color the background.

Finally, another significant metric to assess the quality of the reconstructed conductivity is the dynamic range defined as

$$DR = \frac{\max \sigma^* - \min \sigma^*}{\max \sigma^{GT} - \min \sigma^{GT}} \times 100\%. \quad (44)$$

A DR value which widely differs from 100, indicates that the conductivity contrast was not well preserved in the numerical optimization process.

5.3 Effect of the number of blocks and benefit of the ATV mechanism

To evaluate the effect of the number of blocks K used by the proposed EITGN-NET, we evaluated the performance for varying K values. In particular, we report in Table 1 the quantitative measures MSE and SSIM, averaging the results on the testing set, with $K = \{8, 10, 12\}$. We noticed that the performance is gradually improved for increasing K values and tends to remain stable when K is larger than 10. Therefore the choice $K = 10$ configuration is a preferable setting which represents a good compromise between the result quality and the computational cost.

The conductivity reconstruction quality obtained by EITGN-NET is affected by the new ATV mechanism introduced. To highlight how much this mechanism influences the results, in Fig.5.2 we illustrate the reconstructions produced by the EITGN-NET with ATV (top row) and without activating the ATV stage (bottom row). From a visual inspection we can observe sharper and more artifact-free results when ATV is applied.

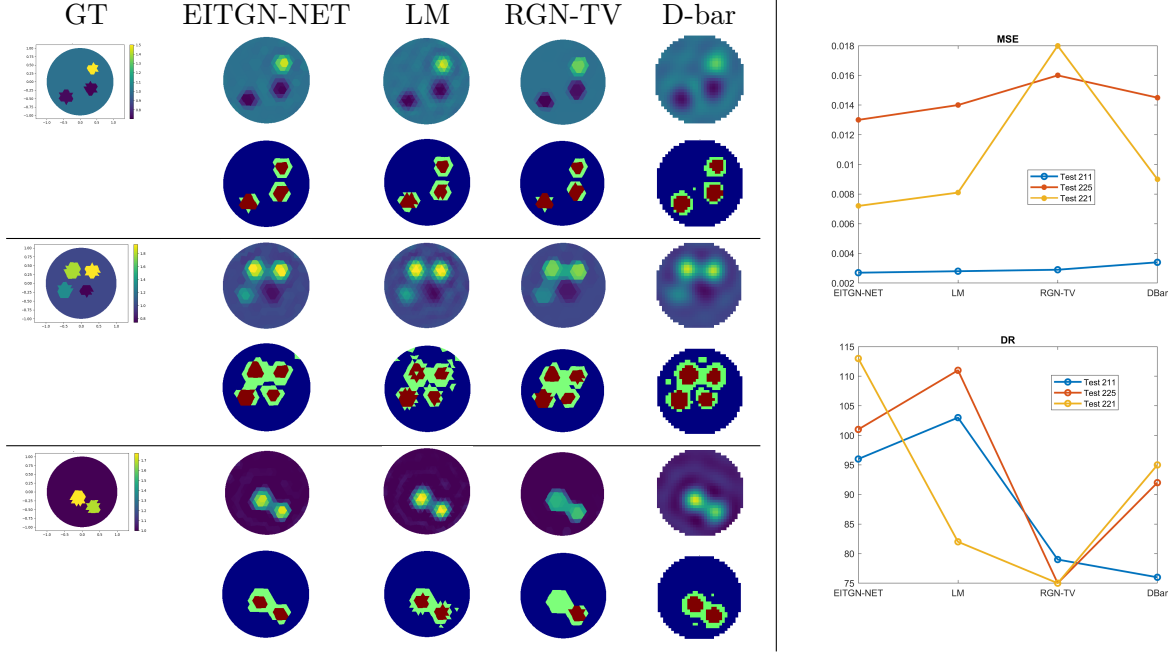


Figure 3: Performance in terms of MSE, DR, EIEI metrics of the reconstructions by EITGN-NET, LM, RGN-TV, and D-bar for test case GT 211, GT 225 and GT 221 (from top to bottom).

	EITGN-NET	LM	DBar	RGN-TV
MSE	0.0037	0.0072	0.0060	0.0038
SSIM	0.89	0.77	0.82	0.93
DR	110	119	107	89

Table 2: Performance on averaged MSE, SSIM, DR metrics on the entire set of test cases.

5.4 Example 1 - Performance comparisons

In Fig.3 we illustrate the performance of EITGN-NET with respect to RGN-TV, LM and D-bar when applied to the reconstruction of three test cases. In Fig.3 (right panel) we plot the graphs corresponding to MSE and DR, while the maps on the left panel visualize the GT, EITGN-NET, RGN-TV, LM and D-bar reconstructions with their associated EIEI maps (bottom row). We recall that, for MSE the lower, the better, while for DR the values closest to 100 are preferred. A qualitative inspection in Fig. 3 (left panel) highlights the superior quality of EITGN-NET which better recovers sharper structures, presents a lower number of artifacts, and in general improves the separation between the anomalies.

By a visual inspection of Fig.4, we can compare σ^{GT} with the reconstructed results obtained by EITGN-NET (σ^* , first column), RGN-TV (second column) and D-bar (third column). The associated EIEI structure maps are illustrated in the bottom rows, yellow for artefacts, red for anomalies and blue for background; the EIEI values are reported for each test case. The test case GT 237 contains 4 anomalies, two of which present intensity values very close to the background value. Nevertheless all the methods are able to detect them properly. The well known contrast reduction effect of the TV regularizer is slightly visible everywhere. In particular, in the test case GT 208, the intensity of the anomalies is significantly reduced by the other methods, while accurately recovered by our network. In general, the EITGN-NET is able to automatically detect all the anomalies with the minimum artifacts,

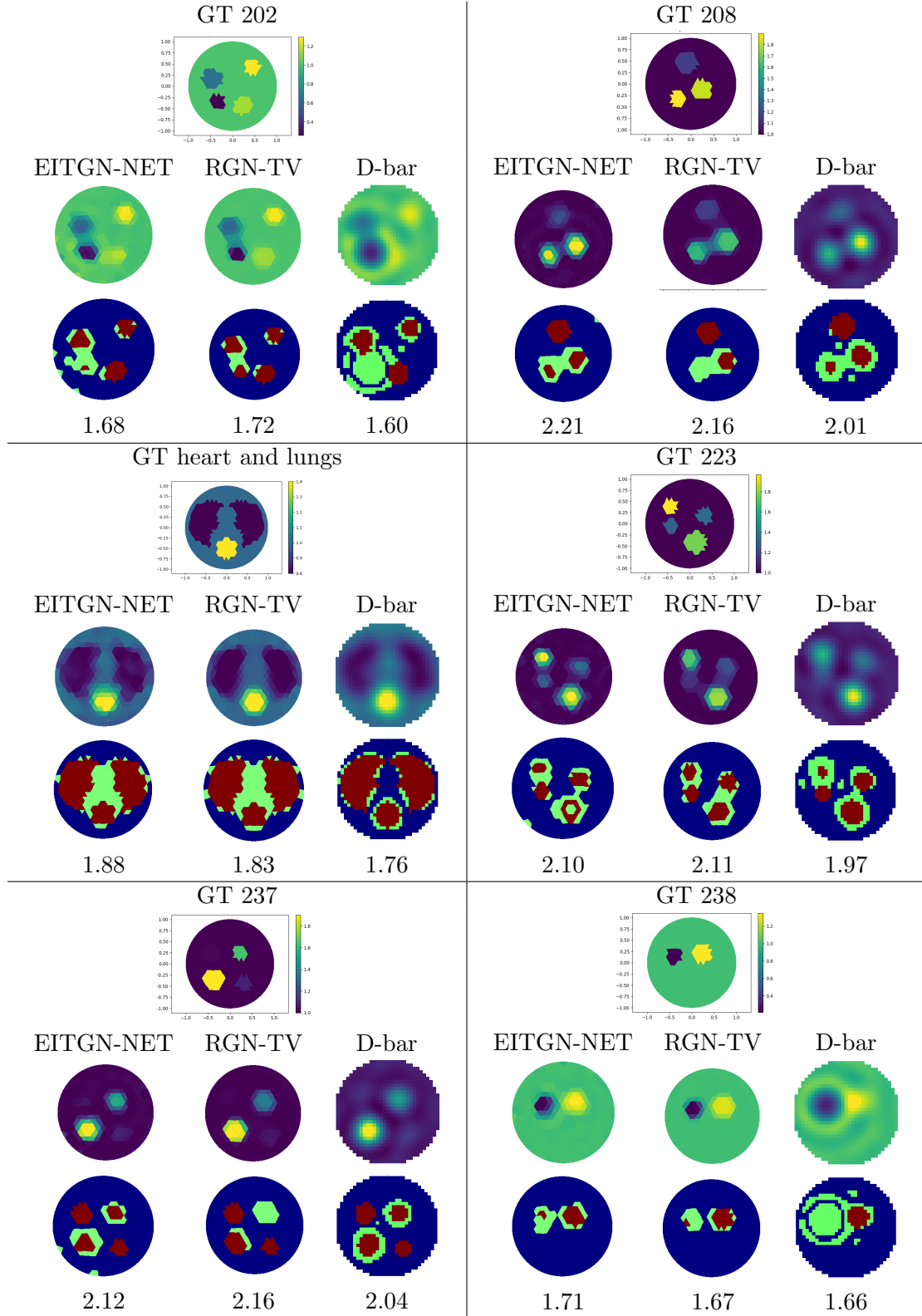


Figure 4: Comparisons between σ^{GT} (top rows) and conductivity results reconstructed by EITGN-NET (first column), RGN-TV (second column) and D-bar (third column) with the associated structure maps (EIEI metric) on the bottom. EIEI values are reported for each test case.

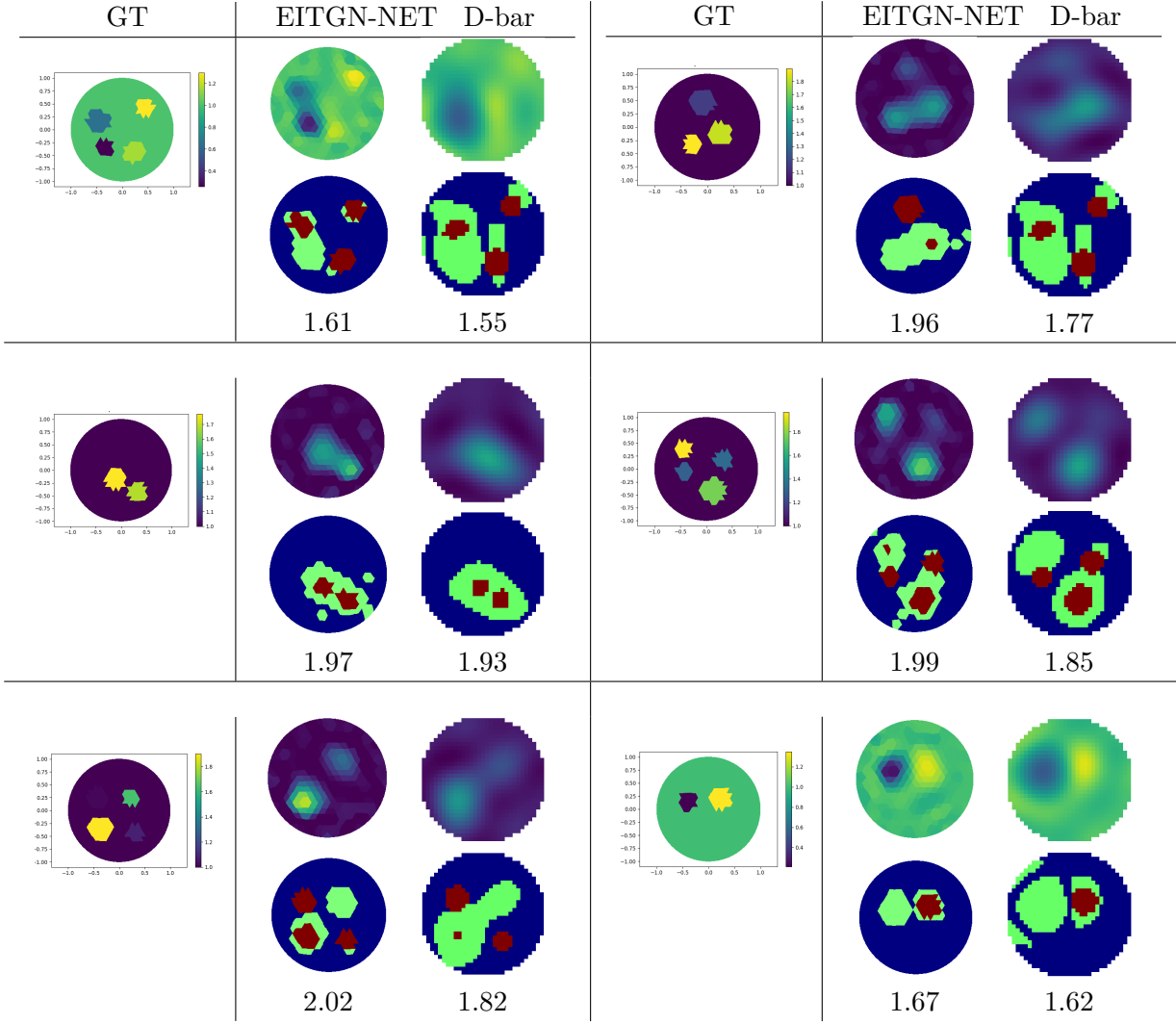


Figure 5: Robustness to the noise: comparison between σ^{GT} and reconstructions from noisy measurements obtained by EITGN-NET (first column) and \bar{D} (second column): the reconstructed conductivities σ^* (first row) and associated structure maps for EIEI metric (second row). EIEI values are reported for each test case.

	EITGN-NET	D-bar
noise 54dB		
MSE	0.0078	0.0107
SSIM	0.75	0.75
DR	102	88
noise 48dB		
MSE	0.0085	0.0111
SSIM	0.67	0.62
DR	110	84

Table 3: Noisy measurements: performance on averaged MSE, SSIM, and DR metrics on the entire set of test cases.

as confirmed by the EIEI values reported below each structure map, while preserving faithfully the anomalies shape and piecewise-constant amplitudes. Performance on averaged MSE, SSIM, and DR metrics on the entire set of test cases are reported in Table 2.

The proposed EITGN-NET has been trained on datasets with circular anomalies. To verify the robustness to other shaped anomalies, we tested different shaped conductivities. By the way of illustration in Fig.4 (case labelled by *heart and lungs*) we report the results of a phantom image representing heart and lungs anomalies which are effectively detected by the proposed network. As expected, the RGN-TV behaves slightly better in this case since the network was trained with different shaped anomalies. This confirms the well-know drawback of the learning-based approaches when the testing dataset is different from what they have been trained with. We trust that, with a suitable training, EITGN-NET will provide more accurate reconstructions even in case of similar anomalies.

5.5 Example 2 - robustness to the noise

The measured voltages are easily contaminated in practical EIT measurements. In order to evaluate the robustness of the proposed method to noisy measurements we corrupted the voltage measurements generated from the solution of the forward model by additive white Gaussian noise. In particular, we generated the noisy measurement vector V_m by adding a vector $\bar{n} \sim \mathcal{N}(0, s^2)$ of Gaussian noise characterized by zero-mean and standard deviation $\eta \bar{V}_m$, with \bar{V}_m the average value. The corresponding degradation model is the following:

$$V_m = V_m + \eta \bar{V}_m \text{rand}(n_M).$$

We trained the network using 50% samples corresponding to corrupted V_m and 50% samples corresponding to noise-free V_m measurements. During the training phase we used $\eta = 5 \times 10^{-3}$ which corresponds to a quality $\text{SNR} = 48\text{dB}$, while we validated the network with two different noise levels $\eta = 2.5 \times 10^{-3}$ ($\text{SNR}=54\text{dB}$) and the more severe $\eta = 5 \times 10^{-3}$ ($\text{SNR}=48\text{dB}$).

The conductivities obtained by the EITGN-NET with noisy measurements ($\text{SNR}=48\text{dB}$) are illustrated in Fig.5 for the test cases reported in Fig.3. The results in Fig.5 show the robustness of the proposed neural network to noise levels up to $\text{SNR}=48\text{dB}$. The results with degradations less severe than $\text{SNR}=48\text{dB}$ are not reported. From a visual comparison of the associated EIEI results we can observe how the noise affects the quality of the reconstructions, slightly corrupting the identification of the different anomalies. We recall that for EIEI metric, the higher, the better. Hence, more severe noise levels demand for new training of the proposed EITGN-NET with a tuning of the α_2 parameter in (22).

To summarize the performance, in Table 3 we report the averaged values on 50 test samples, both for the noise-free test cases, using the network trained without noisy samples, and for the two different degraded input, corresponding to a SNR of 48dB and 54dB. We do not report the results from noisy measures for RGN-TV and LM since for each test case we should have tuned manually the regularization parameter.

The reported metrics confirm the overall better performance of the proposed network.

5.6 Example 3 - Regularizer efficacy

We illustrate the effectiveness of the learned regularizer by checking the behaviours of different popular regularizers with respect to the proposed \mathcal{R}_θ obtained by the network described in Section 4.2. Specifically, we denote by $R_1 = L^T L$ the Laplace regularizer, by $R_2 = \sqrt{\text{diag}(\mathcal{J}^T \mathcal{J})}$ the popular regularizer proposed in NOSER [6], and by R_3 the TV regularizer defined in (12). The averaged condition number of the linear systems (15) during the testing phase is reduced through the network blocks from 10^{21} to 10^7 , thus confirming the benefit of the network regularizer \mathcal{R}_θ .

By the way of illustration we report in Fig.6 four test cases of conductivity reconstructions produced by the Gauss Newton method using as regularizer R_1 , R_2 and R_3 for different regularization parameters λ , together with the EITGN-NET results obtained with the learned regularizer \mathcal{R}_θ . The fully variational RGN method with R_1 , R_2 and R_3 requires the critical selection of the optimal regularization parameter λ to get the best result, which is obtained by manually tuning λ in order to improve the accuracy of the results. We report only three λ values for each regularizer, between them the optimal ones. Unlike, the learned regularizer \mathcal{R}_θ automatically varies itself since it is driven by the data, and thus it is completely parameter free.

The learned regularizers, starting from different settings of initial weights in the FCNN, for the same data set V_m , lead to conductivity reconstructions of the same quality and to a significant improvement of the condition number of the linear system (15) preserving the same order of magnitude. This allows to produce a quasi optimal reconstruction.

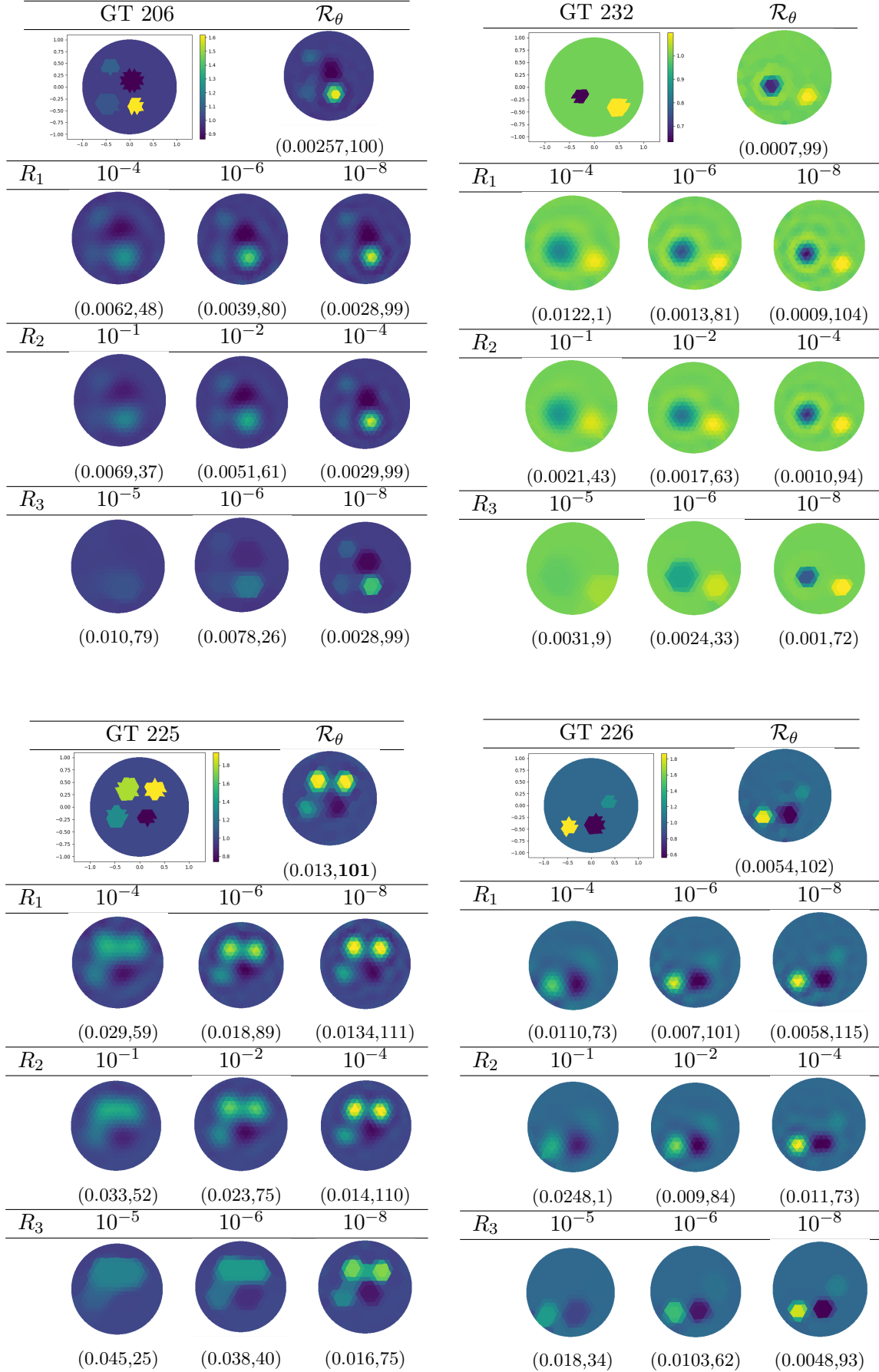


Figure 6: Regularized Gauss-Newton reconstruction results with associated (MSE, DR) values for different regularizers and different λ values together with our learned regularizer \mathcal{R}_θ .

6 Conclusion

In this work, we have proposed a hybrid model-based and data-based method for solving nonlinear EIT inverse problems which exploits a fully connected neural network to learn the regularizer of the Gauss-Newton method from data. Moreover, we proposed an attention-like mechanism, based on anisotropic total variation, which efficacy in piece-wise conductivity reconstructions is demonstrated in the numerical section. This approach was shown to yield higher accuracy with respect to other state-of-the-art approaches for absolute EIT reconstruction (i.e. RGN, D-bar). The extensive testing presented in the previous sections supports this conclusion, that was verified in a number of different configurations: (i) different number of anomalies, (ii) noisy conditions, (iii) heart and lung model, potentially useful for respiration monitoring. While manual hyperparameter tuning and regularizer operator choice is often critical to obtain good reconstruction, in EITGN-NET the regularizer operator is intrinsically tuned, as the training procedure automatically optimizes it for the chosen dataset. Overall, EITGN-NET holds great potential for the integration of model and data-based methods for nonlinear EIT reconstruction, providing a framework for the automation of lengthy, error-prone steps while maintaining explicit modeling constraints that allow for greater interpretability of the reconstruction with respect to end-to-end approaches, a crucial feature for mission-critical fields such as medical imaging.

Acknowledgements

This research was supported in part by the Italian National Group for Scientific Computation (GNCS-INDAM), Research Projects 2020.

References

- [1] A. Borsic, B. M. Graham, A. Adler, and W. R. B. Lionheart. In vivo impedance imaging with total variation regularization. *IEEE Transactions on Medical Imaging*, 29(1):44–54, 2010.
- [2] A. P. Calderón. On an inverse boundary value problem. *Seminar on Numerical Analysis and its Applications to Continuum Physics*, pages 65–73, 1980.
- [3] T. F. Chan, G. H. Golub, and P. Mulet. A nonlinear primal-dual method for total variation-based image restoration. *SIAM Journal on Scientific Computing*, 20(6):1964–1977, 1999.
- [4] X. Chen, Z. Wang, X. Zhang, R. Fu, D. Wang, M. Zhang, H. Wang, and S. Member. Deep Autoencoder Imaging Method for Electrical Impedance Tomography. 70, 2021.
- [5] Z. Chen, Y. Yang, and P.-O. Bagnaninchi. Hybrid learning-based cell aggregate imaging with miniature electrical impedance tomography. *IEEE Transactions on Instrumentation and Measurement*, 70:1–10, 2021.
- [6] M. Cheney, D. Isaacson, J. Newell, S. Simske, and J. Goble. Noser: An algorithm for solving the inverse conductivity problem. *Int. J. Imag. Syst. Technol.*, 2:65–75, 1990.
- [7] K.-S. Cheng, D. Isaacson, J. C. Newell, and D. G. Gisser. Electrode models for electric current computed tomography. *IEEE Transactions on Biomedical Engineering*, 36(9):918–924, Sep. 1989.
- [8] M. Cortesi, A. Samoré, J. Lovecchio, R. Ramilli, M. Tartagni, E. Giordano, and M. Crescentini. Development of an electrical impedance tomography set-up for the quantification of mineralization in biopolymer scaffolds. *Physiological Measurement*, 42(6):064001, 2021.

- [9] Q. Ding, G. Chen, X. Zhang, Q. Huang, H. Ji, and H. Gao. Low-dose ct with deep learning regularization via proximal forward-backward splitting. *Physics in Medicine & Biology*, 65(12):125009, Jun 2020.
- [10] S. J. Hamilton and A. Hauptmann. Deep d-bar: Real-time electrical impedance tomography imaging with deep neural networks. *IEEE Transactions on Medical Imaging*, 37(10):2367–2377, 2018.
- [11] S. J. Hamilton, C. N. Herrera, J. L. Mueller, and A. Von Herrmann. A direct D-bar reconstruction algorithm for recovering a complex conductivity in 2D. *Inverse Problems*, 28(9), 2012.
- [12] S. J. Hamilton, A. Hänninen, A. Hauptmann, and V. Kolehmainen. Beltrami-net: domain-independent deep d-bar learning for absolute imaging with electrical impedance tomography (a-EIT). *Physiological Measurement*, 40(7):074002, jul 2019.
- [13] M. Huska, D. Lazzaro, and S. Morigi. A forward-backward strategy for handling non-linearity in electrical impedance tomography. In O. Gervasi and et al., editors, *Lecture Notes in Computer Science (vol 12951) Computational Science and Its Applications – ICCSA 2021*, pages 635–651, Cham, 2021. Springer International Publishing.
- [14] M. Huska, D. Lazzaro, S. Morigi, A. Samoré, and G. Scrivanti. Spatially-adaptive variational reconstructions for linear inverse electrical impedance tomography. *J. Sci. Comput.*, 84:46, 2020.
- [15] Y. Li and S. Osher. A new median formula with applications to PDE based denoising. *Communications in Mathematical Sciences*, 7(3):741 – 753, 2009.
- [16] W. R. Lionheart. EIT reconstruction algorithms: Pitfalls, challenges and recent developments. In *Physiological Measurement*, 2004.
- [17] B. Liu, B. Yang, C. Xu, J. Xia, M. Dai, Z. Ji, F. You, X. Dong, X. Shi, and F. Fu. pyeit: A python based framework for electrical impedance tomography. *SoftwareX*, 7:304–308, 2018.
- [18] P. H. Martins, V. Niculae, Z. Marinho, and A. F. T. Martins. Sparse and structured visual attention. *ArXiv*, abs/2002.05556, 2020.
- [19] J. L. Mueller and S. Siltanen. *Linear and Nonlinear Inverse Problems with Practical Applications*. Society for Industrial and Applied Mathematics, Philadelphia, PA, 2012.
- [20] P. A. Muller, J. L. Mueller, M. Mellenthin, R. Murthy, M. Capps, B. D. Wagner, M. Alsaker, R. Deterding, S. D. Sagel, and J. Hoppe. Evaluation of surrogate measures of pulmonary function derived from electrical impedance tomography data in children with cystic fibrosis. *Physiological Measurement*, 39(4):045008, 2018.
- [21] J. M. Ramirez, J. I. M. Torre, and H. Arguello. Ladmm-net: An unrolled deep network for spectral image fusion from compressive data. *Signal Processing*, 189:108239, 2021.
- [22] T. Rymarczyk, E. Kozłowski, G. Kłosowski, and K. Niderla. Logistic regression for machine learning in process tomography. *Sensors (Switzerland)*, 19(15):1–19, 2019.
- [23] F. Santosa and M. Vogelius. A backprojection algorithm for electrical impedance imaging. *SIAM Journal on Applied Mathematics*, 50(1):216–243, 1990.
- [24] S. Stefanescu, C. Schlumberger, and M. Schlumberger. Sur la distribution électrique potentielle autour d’une prise de terre ponctuelle dans un terrain à couches horizontales, homogènes et isotropes. *Journal de Physique et le Radium*, (1(4)):132–140, 1930.

- [25] T. N. Tallman and D. J. Smyl. Structural health and condition monitoring via electrical impedance tomography in self-sensing materials: A review. *Smart Materials and Structures*, 29(12), 2020.
- [26] M. Vauhkonen, D. Vadasz, P. A. Karjalainen, E. Somersalo, and J. P. Kaipio. Tikhonov regularization and prior information in electrical impedance tomography. *IEEE Transactions on Medical Imaging*, 17(2):285–293, April 1998.
- [27] H. Wang, C. Wang, and W. Yin. A pre-iteration method for the inverse problem in electrical impedance tomography. *IEEE Transactions on Instrumentation and Measurement*, 2004.
- [28] Z. Wang, S. Yue, K. Song, X. Liu, and H. Wang. An unsupervised method for evaluating electrical impedance tomography images. *IEEE Transactions on Instrumentation and Measurement*, 67(12):2796–2803, 2018.
- [29] Z. Wei and X. Chen. Induced-current learning method for nonlinear reconstructions in electrical impedance tomography. *IEEE Transactions on Medical Imaging*, 39(5):1326–1334, 2020.
- [30] Q. Yang, A. Sadeghi, G. Wang, G. B. Giannakis, and J. Sun. Gauss-Newton Unrolled Neural Networks and Data-driven Priors for Regularized PSSE with Robustness. *arXiv e-prints*, page arXiv:2003.01667, Mar. 2020.